Materials
Advances

ROYAL SOCIETY
OF CHEMISTRY

PAPER

View Article Online
View Journal | View Issue

Check for updates

Cite this: *Mater. Adv.*, 2022, 3, 8157

Impact of the sintering additive Li_3PO_4 on the sintering behaviour, microstructure and electrical properties of a ceramic LATP electrolyte†

Matthias Rumpel, *[a] Lavinia Appold,[a] Jens Baber,[b] Werner Stracke,[a] Andreas Flegler[a] and Gerhard Sextl[a]

Received 8th June 2022,
Accepted 23rd August 2022

DOI: 10.1039/d2ma00655c

rsc.li/materials-advances

Competitive all solid-state batteries (ASSBs) require particulate, ternary composite cathodes, consisting of a ceramic active material, ceramic solid-state electrolyte (SSE) and an electrical conductor, to achieve high energy densities. Firmly bonded contacts between the active material and SSE are necessary to obtain fast Li-ion transfer, so that sintering processes are unavoidable. Since the sintering temperatures of oxidic ceramic SSEs, such as $Li_{1+x}Al_xTi_{2-x}(PO_4)_3$ (LATP), are above 950 °C, decomposition and mixed phase formation take place during sintering with active materials, so a reduction of the SSE's sintering temperature is necessary. This study investigates the impact of Li_3PO_4 (3, 5 and 10 vol%) as a sintering additive on the sintering behaviour, microstructure and electrical properties of LATP. The obtained liquid phase sintering results in the acceleration of the densification process, so that the start of sinter neck formation and shrinkage could be reduced by 50 °C and 150 °C, respectively. Effects related to the sintering process, such as $LiTiOPO_4$ and $AlPO_4$ formation, densification, grain size distribution and crack formation, are correlated with the electrical properties. Microscopic effects like changes in the lattice stoichiometry and nature of the grain boundary as well as macroscopic effects like pores, grain sizes and cracks have an influence on the percolation network for Li-ion migration. Finally, the addition of Li_3PO_4 to LATP results in a high ionic conductivity of *ca.* 2×10^{-4} S cm^{-1} along with a reduced sintering temperature of 800 °C.

Introduction

The development of all solid-state batteries (ASSBs) is a promising approach to address present and future challenges in the energy storage sector. The application profiles for electromobility and stationary energy storage for renewable energies or consumer products such as smartphones and laptops demand higher energy density, longer cycle life, and better cycling stability along with higher safety.[1–8] These requirements, theoretically, can be achieved by replacing the flammable organic liquid electrolyte used in conventional lithium-ion batteries with a solid-state electrolyte, such as a Li-ion conductive ceramic. As a result, the risk of leakage of the liquid component can be eliminated and without the use of flammable components, the safety can be significantly increased. The energy density can be increased by ceramic electrolytes due to their higher potential window, which enables high voltage active materials, and the possibility to use lithium metal anodes.[9–11] $Li_{1+x}Al_xTi_{2-x}(PO_4)_3$ (LATP), for instance, exhibits high electrochemical stability against oxidation up to 5 V *vs.* Li/Li^+, so a lower degradation of high voltage active materials is expected.[10,11] Since the stiff and dense microstructure of the ceramics inhibits dendrite growth, it is possible to implement lithium metal anodes, which have a specific capacity that is ten times higher than that of the conventionally used graphite.[12] Particulate layers consisting of a ceramic active material, a ceramic electrolyte and an electrically conductive additive are necessary to form a solid-state cathode. However, a fast charge transfer or lithium hopping between the electrolyte and active material as well as between the electrolyte particles requires firmly bonded contacts between the grains of the ternary composite. This requirement makes sintering unavoidable. However, during high temperature treatments, interdiffusion processes cause decomposition and the formation of mixed phases, which causes significant performance losses of the cathode.[13–15]

Reducing the sintering temperature is one possibility to inhibit these phenomena, which may lead to the additional benefit of reduced production cost and lower CO_2 emissions

---

[a] *Fraunhofer Institute for Silicate Research ISC, Center for Electromobility, Neunerplatz 2, 97082 Wuerzburg, Germany*
[b] *Fraunhofer Institute for Silicate Research ISC, Center for High Temperature Materials and Design HTL, Gottlieb-Keim-Str. 62, 95448 Bayreuth, Germany*

† Electronic supplementary information (ESI) available. See DOI: **https://doi.org/10.1039/d2ma00655c**

during manufacturing. Sintering additives can be used to reduce the sintering temperature by utilizing liquid phase sintering, which accelerates the sintering and densification processes. The additive must have a lower melting temperature than the sintering temperature of the host material. The resultant liquid phase enhances particle rearrangement, mass transport and diffusion, so that densification and grain growth are enhanced at lower sintering temperatures, which additionally influence the microstructure of the host material.[16–19]

Several studies have already demonstrated the impact of the microstructure of ionic conducting ceramics on the electrical properties such as ionic conductivity.[20–27] Hupfer *et al.* could improve the ionic conductivity by a decrease of the sintering time of LATP at 1100 °C.[20] The authors correlated the conductivity enhancement with smaller grain sizes, fewer cracks and the grain lattice orientation. The importance of grain size on the overall ionic conductivity has also been calculated by means of the brick layer model.[28–33] Bouchet *et al.* calculated a significant increase in ionic conductivity by reducing the grain size from 500 nm to 5 nm due to a higher amount of Li-ion migration parallel to the grain boundaries.[28] Indris *et al.* compared nanocrystalline and microcrystalline Li_2O:B_2O_3 composites and demonstrated higher conductivity of the nanocrystalline material despite a higher amount of non-conductive B_2O_3. The authors attribute this to a higher amount of defects at the grain boundaries, and thus, faster ion diffusion along the grain boundaries.[21] Along with the grain size, further macroscopic properties like porosity and cracks might influence the percolating network for Li-ion migration. Additionally, microscopic effects like grain lattice orientation and the nature of grain boundaries affect the electrical properties. Ma *et al.* could identify low-angle and high-angle grain boundaries in $Li_{3x}La_{2/3-x}TiO_3$ (LLTO).[34] The angle between two neighbouring grain lattices defines the degree of misorientation at the grain boundary, which correlates with the grain boundary energy.[18] Higher grain boundary energies imply higher barriers for Li-ion hopping between grains, so that it results in higher activation energy for the Li-ion migration process. Consequently, the sintering behaviour affects grain size, porosity, cracks and the nature of the grain boundaries, which is supposed to be changed by the sintering additives.

Some effects of sintering additives on the electrical properties have been previously demonstrated.[35–42] These studies have shown that sintering additives change the nature of grain boundaries, which causes an increase in activation energy.[36,37,40,41] Hupfer *et al.* reported an increase in ionic conductivity of LATP by adding $LiTiOPO_4$ in combination with sintering temperatures of up to 925 °C.[38] Waetzig *et al.* gave an overview of various sintering additives, such as Li_3PO_4, Li_3BO_3 and Li_2CO_3, and their impact on the sintering temperature of LATP. Ionic conductivities comparable to pure LATP sintered at 1100 °C could be achieved by sintering at 800 °C.[42]

This study takes a more detailed look into the influence of lithium phosphate (Li_3PO_4) on the sintering behaviour, microstructure and electrical properties of LATP. Since the melting point of Li_3PO_4 (837 °C[43]) is below that of the sintering temperature range of LATP (>900 °C[20,27]), liquid phase sintering is expected. Various amounts of Li_3PO_4 powder were mixed with the LATP powder and sintered at various temperatures up to 950 °C. As the goal of this work is to reduce the sintering temperature, the focus lies mainly on the lower end of the sintering temperature range. The sintering temperature is reduced by at least 200 °C as evaluated by the comparison of grain boundary conductivities. Finally, a correlation of sintering behaviour, microstructure and electrical properties is demonstrated.

Experimental

Powder preparation

The $Li_{1.3}Al_{0.3}Ti_{1.7}(PO_4)_3$ powder was synthesized *via* a sol–gel route by dissolving stoichiometric amounts of lithium acetate dihydrate, aluminium nitrate nonahydrate and ammonium dihydrogen phosphate in a 1 : 1 mixture of ethanol and 1-methoxy-2-propanol, to which concentrated nitric acid was added. Titanium(IV) butoxide was mixed with acetylacetone in a second vessel for 30 min in order to guarantee complete complex formation. Afterwards, the two solutions were mixed and stirred for a further 30 min. The sol was dried until an orange amorphous powder was obtained. The powder was ground in a mortar and then crystallized for 5 h at 800 °C in an alumina crucible. Finally, the crystallized LATP powder was ball-milled at 400 rpm for 40 min. The particle size distribution was 200– 600 nm (Fig. S1, ESI†). Various amounts (3, 5 and 10 vol%) of Li_3PO_4 (SigmaAldrich®, CAS: 10377-52-3) were added and mixed using a speed mixer (DAC 400.1 VAC-P, Hauschild®) for 10 min at 1000 rpm.

Characterization of sintering behaviour

The sintering behaviour, *i.e.* densification, shrinkage and porosity, was characterized using a thermal-optical measurement device (TOM) and water saturation based on the Archimedes principle. Pellets of pure LATP powder and LATP + 5 vol% Li_3PO_4 powder were pressed with 2000 kN. The diameter and thickness of the green body were 11 mm and *ca.* 2 mm, respectively. These pellets were characterized using a TOM, which enables *in situ* measurement of shrinkage and thermal diffusivity during the sintering process. Further information about the TOM system can be found in the publications of the F. Raether group.[44–48] Thermal diffusivity was measured by a laser flash technique using a CO_2-TEA laser and a pyrometer on the back side of the sample. The shrinkage was measured using an optical dilatometer. The heating rate was 5 K min^{-1}. Thermal diffusivity and pellet thickness were measured every 50 °C. The final sintering temperatures were between 650 °C and 950 °C. The sintering duration was 24 h in the holding step. Afterwards the furnace cooled down at a rate of *ca.* 2 K min^{-1}. After TOM characterization, the pellets were characterized by water saturation based on the Archimedes principle to obtain porosity.

Characterization of crystalline phases and microstructure

X-Ray diffraction (XRD) on the pellets sintered at 900 °C was performed using a PANalytical Empyrean diffractometer with CuKa radiation at 2θ values between 15° and 60° with a step size of 0.02° and a scan duration per step of 5 s. A Bragg–Brentano geometry with a plane sample and a moving X-ray source and detector ($\theta:\theta$ scan) were used. The powder sample rotated around its axis in order to average the impact of various crystal orientations.

Scanning electron microscopy (SEM) images were collected using a ZEISS AURIGA 60 microscope with an accelerating voltage of 5 kV and a backscattered electron detector. The preparation of the cross-sections was done by polishing the pellets with a JEOL SM-0910 cross-section polisher under an argon atmosphere. The lower and upper limits of the range of the grain sizes were determined by means of the ImageJ® software. EDS spectra were recorded using an AMETEK EDAX Octane Elect Plus analytical system.

Characterization of electrical properties

Electrical impedance spectroscopy (EIS) was performed on pellets prepared from pure LATP powder and powder mixtures with 3 vol%, 5 vol% and 10 vol% Li_3PO_4. 0.5 g of the powders were pressed at 80 kN into pellets. The green body thickness was approximately 1.4 mm and the diameter was 16 mm. The same sintering conditions used for TOM analysis were applied in a muffle furnace (P330, Nabertherm). An alumina crucible was used. The pellets were sputtered with gold contacts (diameter 10 mm) and then dried under vacuum (10^{-2} mbar) at 120 °C for 10 h. Pouch cells were assembled in an argon-filled glovebox ($H_2O < 1$ ppm and $O_2 < 1$ ppm) in order to avoid humidity during the EIS measurement. EIS measurements were carried out with a galvanostat (VMP-300, Biologic) at room temperature (25 °C). The frequency range was 7 MHz to 1 Hz and the amplitude was 50 mV. All measurements, including sample preparation, were carried out in triplicate. Since good reproducibility could be achieved, one representative pellet of each sintering parameter set was measured by temperature-dependent EIS in the temperature range between −20 °C and 60 °C in 10 °C steps. The pellets of the pure LATP and LATP + 5 vol% Li_3PO_4 were subsequently used to determine the microstructure by SEM.

Results and discussion

$LiTiOPO_4$ and $AlPO_4$ formation

The phase compositions of all powder mixtures sintered at 900 °C were analysed by XRD. The XRD pattern intensities were normalized to that of the main LATP reflection at 24.52° (Fig. 1). In addition to the crystalline LATP reflections (ICSD 95979), $LiTiOPO_4$ (ICSD 153522) could be detected at 27.04°, 27.42°, 27.85° and 27.95° as well as $AlPO_4$ (ICSD 44880) could be detected at 20.62° for Li_3PO_4-containing LATP samples. The $LiTiOPO_4$ and $AlPO_4$ intensities increase with a higher amount of Li_3PO_4. Li_3PO_4 cannot be detected.

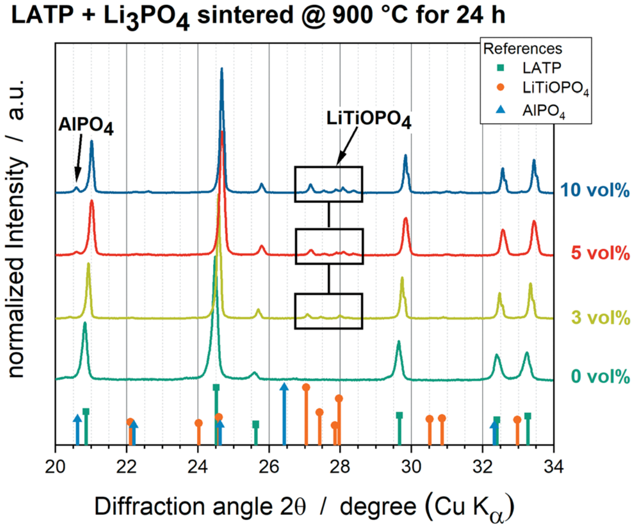

Fig. 1 XRD patterns of all powder mixtures sintered at 900 °C. Pure LATP (dark green), LATP + 3 vol% Li_3PO_4 (light green), LATP + 5 vol% Li_3PO_4 (red) and LATP + 10 vol% Li_3PO_4 (blue).

The formation of the secondary phases $LiTiOPO_4$ and $AlPO_4$ could additionally be confirmed by EDS analyses of the SEM cross section of the LATP + 5 vol% Li_3PO_4 pellet sintered at 950 °C (Fig. 2). Four different contrasts for grains are distinguishable (Fig. 2a), which can be correlated with LATP (Pos 1), $LiTiOPO_4$ (Pos 2), $AlPO_4$ (Pos 3) and Li_3PO_4 (Pos 4) by means of EDS analyses (Fig. 2b). Precipitates of $LiTiOPO_4$ and $AlPO_4$ appear at the interfaces of Li_3PO_4 and LATP.

The formation of $AlPO_4$ and $LiTiOPO_4$ as well as further impurity phases, such as TiO_2, due to the decomposition of pure LATP is well reported in the literature as impurity phases, which can be formed at sintering temperatures above 900 °C and caused by stoichiometric imbalances during synthesis.[20,26,49,50] Since the pure LATP pellet sintered at 900 °C appears highly free from impurity phases in the XRD diffractograms (Fig. 1), it can be deduced that the addition of Li_3PO_4 induces the formation of secondary phases or reduces the temperature of the decomposition process of LATP. Furthermore, the pellets with a higher Li_3PO_4 amount show increased intensities for the $AlPO_4$ and $LiTiOPO_4$ reflections, which indicates a correlation between the Li_3PO_4 amount and the amount of the secondary phases.

Pore elimination, densification and shrinkage

Pore elimination, densification and shrinkage processes occur in parallel during sintering to result in a compact microstructure. Pore elimination and densification are characterized by porosity and thermal diffusivity. The latter is a measure of the heat transport through the material due to elastic vibrations of the lattice. The thermal diffusivity is enhanced by more grain to grain contacts, so that it is a measure for the degree of pore elimination and densification. Shrinkage is described by the reduction of the relative thickness of the pellet. The TOM analyses of all samples can be found in the ESI,† (Fig. S2). Since all samples show the same trend, representative samples

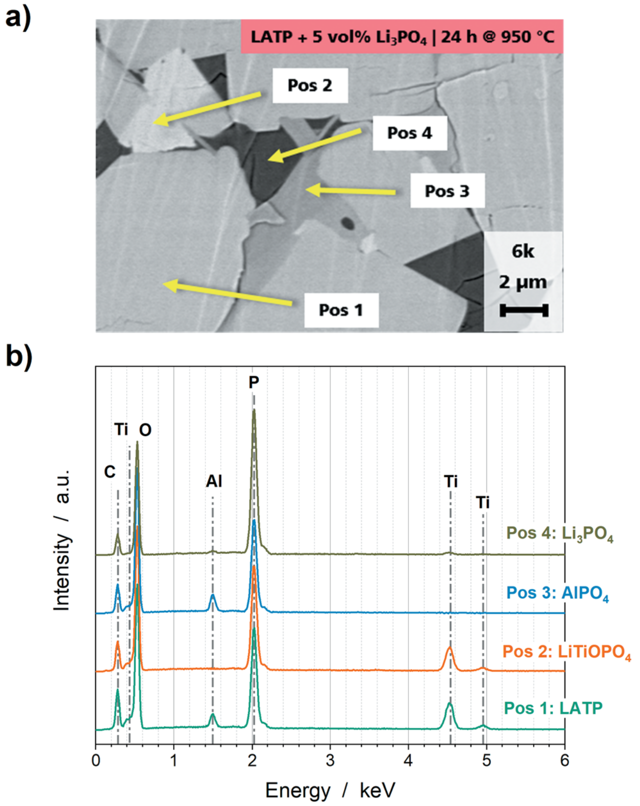

Fig. 2 (a) SEM cross section and (b) corresponding EDS analyses of a LATP + 5 vol% Li_3PO_4 pellet sintered at 950 °C for 24 h.

of pure LATP and LATP + 5 vol% Li_3PO_4 sintered at 900 °C are presented in Fig. 3. A first increase of the thermal diffusivity is observed between 600 °C and 650 °C for pure LATP and between 550 °C and 600 °C for LATP + 5 vol% Li_3PO_4. This increase in the thermal diffusivity corresponds to the sinter neck formation, so its temperature is reduced by 50 °C with Li_3PO_4. A continuous increase can be detected for the pure LATP pellet until the end of the holding step; during the holding step at 900 °C, the thermal diffusivity increases from 0.07 $mm^2\ s^{-1}$ to 0.38 $mm^2\ s^{-1}$. A similar trend is seen with the pure LATP sample sintered at 950 °C (Fig. S2, ESI†). In contrast, the thermal diffusivity values of the LATP + 5 vol% Li_3PO_4 sample undergo a rapid increase up to 800 °C and then remain constant during the holding step. All LATP + 5 vol% Li_3PO_4 samples sintered at temperatures ≥800 °C show the same trend and end value of *ca.* 0.47 $mm^2\ s^{-1}$. The largest increase of the sample LATP + 5 vol% Li_3PO_4 sintered at 750 °C occurs during the holding step, but reaches the same end value (Fig. S2, ESI†).

Since the densification process and shrinkage take place simultaneously, the curves of the relative thicknesses show the opposite trend (Fig. 3). Pure LATP pellets show shrinkage during the holding step even at 950 °C. The LATP + 5 vol% Li_3PO_4 samples reach a maximum shrinkage of *ca.* 13.6% at 800 °C; this value remains constant even with higher sintering temperatures. The start of shrinkage can be determined to be 800–850 °C for the pure LATP pellet and at 650–700 °C for the LATP + 5 vol% Li_3PO_4 pellet.

Since the changes in the thermal diffusivities correspond to pore elimination and densification, the trend of their end values can be correlated with the porosities measured after the sintering processes. The porosities are compared with the end values of shrinkage as a function of sintering temperature in Fig. 4. Pure LATP shows a steady increase and decrease of shrinkage and porosity, respectively, with the sintering temperature. These values at 950 °C are 5.3% and 33%, respectively. In contrast, the LATP + 5 vol% Li_3PO_4 sample sintered at 800 °C shrank most by 13.6% and had a lowest porosity of 6.8%. At sintering temperatures ≥850 °C, the porosity slightly increases to 9.6%, which corresponds to the crack formation discussed below.

The trends during the densification process of the Li_3PO_4-containing LATP samples can be categorized into the three sintering stages, well known from the literature.[16–19] The first stage at 650 °C is attributed to particle reorganization and sinter neck formation. Pore elimination dominates the intermediate sintering stage, which takes place between 650 °C and 750 °C. Since the samples sintered at 750 °C show an increase in thermal diffusivity and ongoing shrinkage during the holding step, this temperature can be considered as the transition from the intermediate to the final stage. Pore elimination is completed in the final stage, which starts at *ca.* 750 °C; therefore, grain growth is the dominant process. In contrast, a plateau in the porosity and shrinkage is not detected for the pure LATP pellets, which indicates that the final stage has not yet been reached. This is confirmed by the publications of Hupfer *et al.*[20] and Waetzig *et al.*,[27] who stated that most of the shrinkage of pure LATP occurs between 950 °C and 1100 °C.

Grain growth and crack formation

Grain growth takes place during all sintering stages. Cracks can appear due to internal stresses during sintering provoked by ongoing grain growth as well as by relaxation of the material during cooling due to locally different shrinkage gradients within the microstructure. The SEM images of the cross sections of the pure LATP and LATP + 5 vol% Li_3PO_4 samples are shown in Fig. 5. The grain size distributions of the pure LATP pellets are 4–8 µm (850 °C), 10–50 µm (900 °C) and >60 µm (950 °C). Additionally, cracks and a high amount of pores can be detected at 900 °C and 950 °C (Fig. 5b and c). In contrast, the LATP + 5 vol% Li_3PO_4 samples have grain size distributions of 0.3–6 µm (650 °C), 2–6 µm (700 °C), 5–15 µm (750 °C), 6–18 µm (800 °C), 8–22 µm (850 °C) and 8–25 µm (900 °C) (Fig. 5d–i). The pellet sintered at 950 °C shows the same range of grain sizes as that sintered at 900 °C, but with a higher amount of large grains (Fig. 5j), which indicates that a maximum of grain growth is reached at 900 °C. Cracks appear at 850 °C and their amount increases with higher sintering temperatures. In the first sintering stage at 650 °C, sinter necks can be observed between grains with grain sizes of *ca.* 300 nm, which is similar to the initial powder particle size (Fig. S1, ESI†). Open pore channels are detected at 700 °C, which corresponds to the intermediate stage. Pore elimination is completed at 750 °C, where a dense

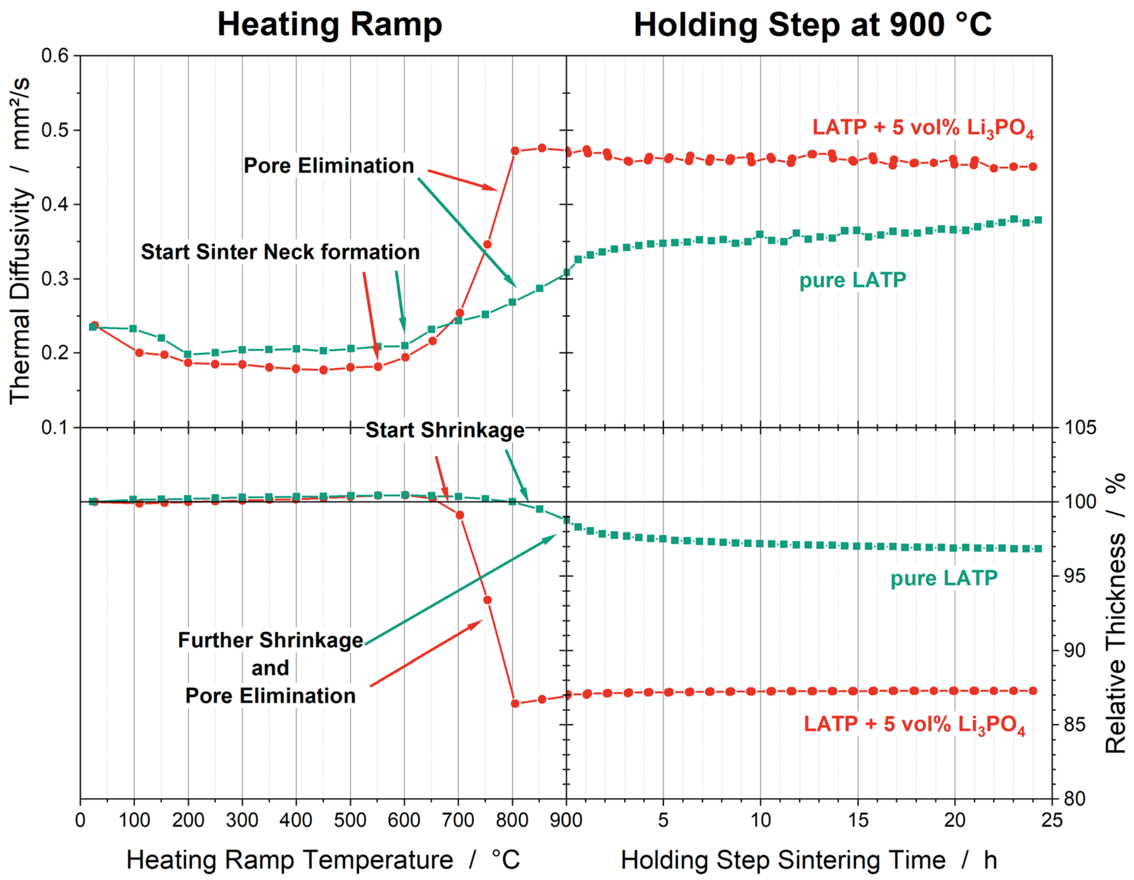

Fig. 3 Thermal diffusivities and relative densities of the pure LATP (green) and LATP + 5 vol% Li_3PO_4 (red) pellets sintered at 900 °C. The heating ramp is plotted as a function of temperature; the holding step is plotted as a function of time. The trends during the heating ramp are representative of all pellets of the same composition (Fig. S2, ESI†).

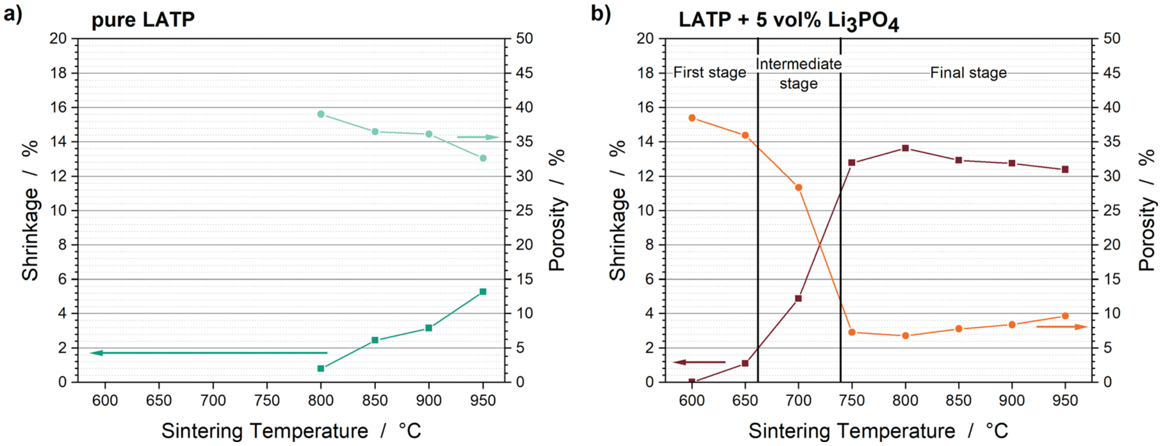

Fig. 4 Shrinkages at the end of sintering and porosities as a function of the sintering temperatures of (a) the pure LATP samples and (b) LATP + 5 vol% Li3PO4 samples.

microstructure can be seen. Grain growth based on Ostwald ripening takes place in the final sintering stage starting at 750 °C. Large grains grow by incorporating smaller grains, which results in a microstructure of large grains surrounded and connected by smaller ones. The Li_3PO_4 is well dispersed in the pores or triple points between the grains. The size of the Li_3PO_4 regions also increases with the sintering temperature. However, it cannot be detected in the direct contact area or grain boundaries between two neighbouring grains. Precipitates of $LiTiOPO_4$ and $AlPO_4$ also grow with sintering

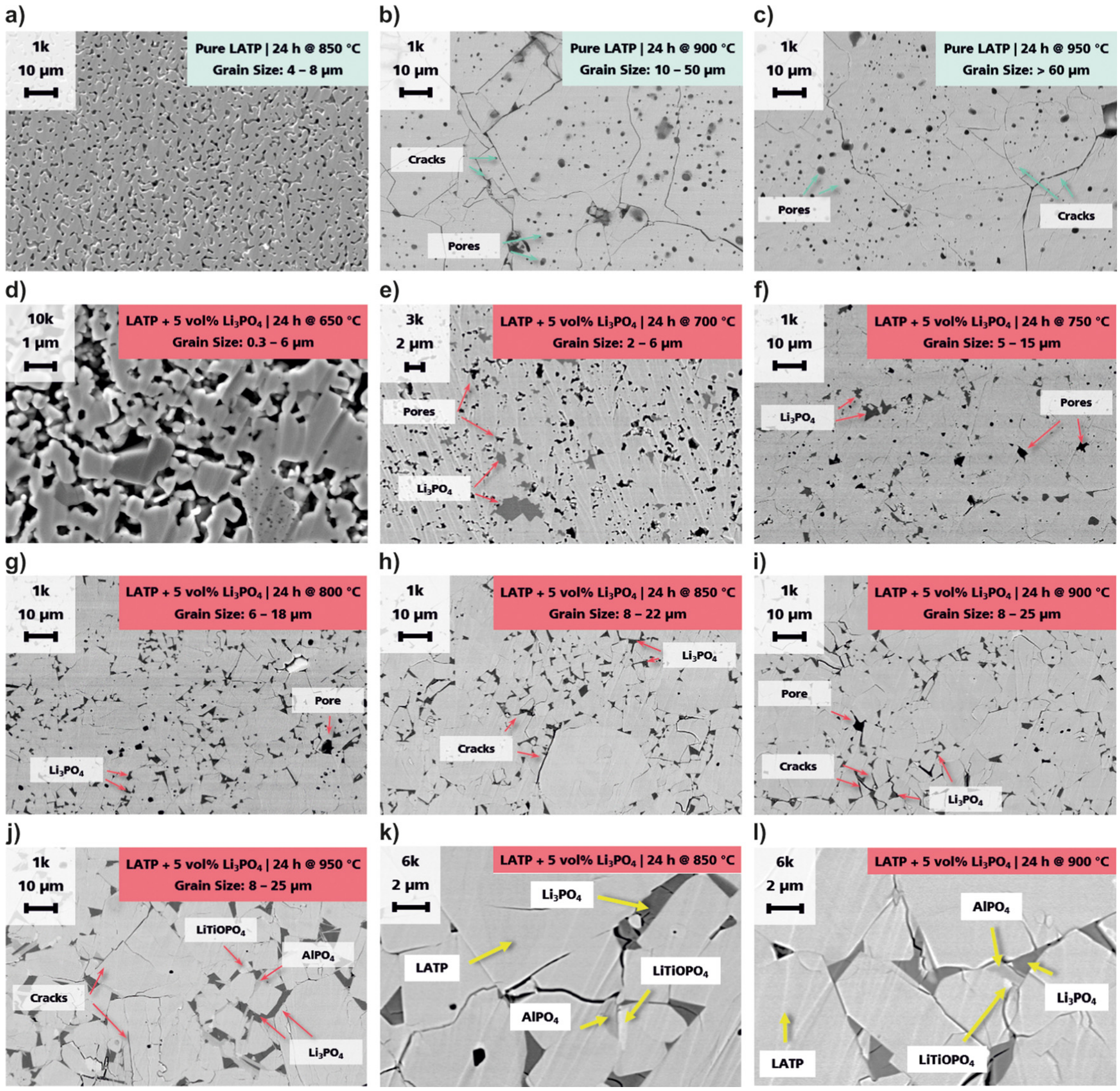

Fig. 5 SEM cross sections of the pure LATP samples sintered at (a) 850 °C, (b) 900 °C and (c) 950 °C and LATP + 5 vol% Li_3PO_4 samples sintered at (d) 650 °C, (e) 700 °C, (f) 750 °C, (g) 800 °C, (h) and (k) 850 °C, (i) and (l) 900 °C and (j) 950 °C. The sintering time was 24 h. The accelerating voltage was 5 kV. A backscattered electron detector was used to obtain a higher contrast.

temperature so that grains of about 1 µm are evident for the LATP + 5 vol% Li_3PO_4 sample annealed at 950 °C, whereas a smaller precipitate size can be detected for the 850 °C and 900 °C samples at higher magnifications (Fig. 5k and l). This additionally suggests an enhanced decomposition process of LATP along with increased formation of secondary phases at high sintering temperatures.

Electrical properties and their correlation with the sintering behaviour and microstructure

In addition to the pure LATP pellets and the LATP + 5 vol% Li_3PO_4 pellets, LATP pellets with 3 vol% and 10 vol% Li_3PO_4 were prepared for EIS. The Nyquist plots of all samples demonstrate a clear semicircle, which is related to the grain boundary conduction process (Fig. 6a). At first glance, the total resistances of the Li_3PO_4-containing samples appear to be about half that of the pure LATP. The equivalent circuit shown in Fig. 6b was used to fit the EIS data to obtain the resistances for bulk (R_b) and grain boundary (R_{gb}) migration, as well as the grain boundary capacitances C_{gb}. Considering the thickness d of the pellet and the electrode area A, the bulk conductivity σ_b and the grain boundary conductivity σ_{gb} can be calculated using the equations:

$$\sigma_b = \frac{1}{R_b} \cdot \frac{d}{A} \text{and } \sigma_{gb} = \frac{1}{R_{gb}} \cdot \frac{d}{A}$$

Furthermore, the activation energies associated with the grain boundary conductivity, $E_{a,gb}$, which is a measure of the barrier of Li-ion hopping from one grain to another, can be evaluated by temperature-dependent EIS measurements using the Arrhenius plots. The corresponding plots can be found in the ESI† (Fig. S3). The activation energy is obtained by fitting the data with the Arrhenius equation:

$$\ln \sigma_{gb} T = -\frac{E_{a,gb}}{k_b} \cdot \frac{1}{T} + \ln B$$

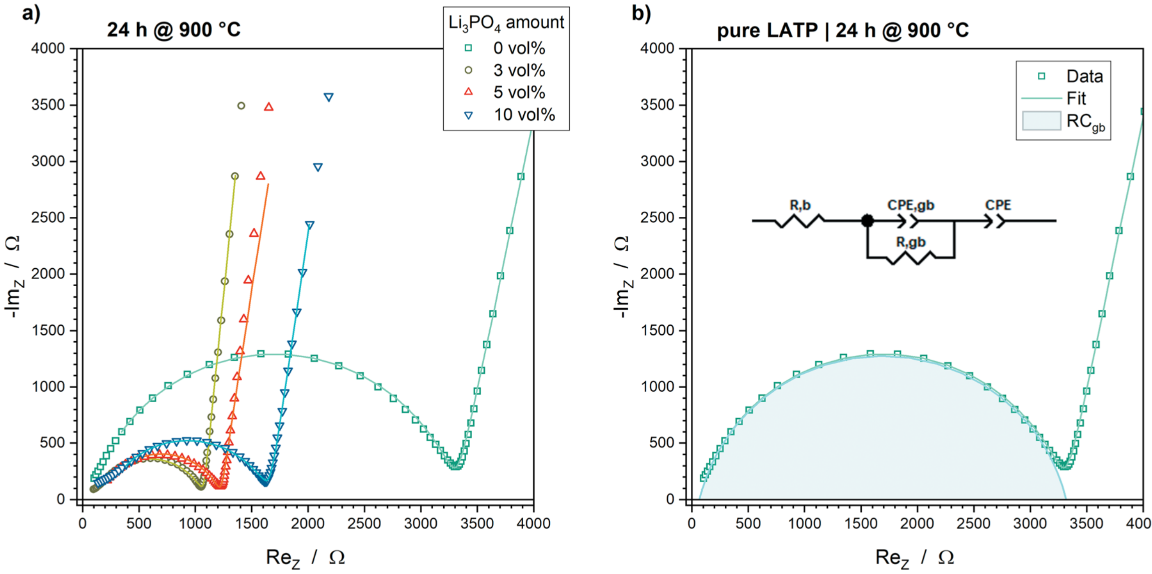

Fig. 6 Nyquist plots including fits of (a) samples sintered at 900 °C for 24 h. (b) Fit of EIS data of the pure LATP pellets sintered at 900 °C for 24 h. The equivalent circuit given in the inset was used to fit all data.

where T is the temperature, and k_b is the Boltzmann constant. The value B includes many further parameters such as diffusivity or defect concentration.

The values of bulk conductivity as well as grain boundary conductivity, capacitance and activation energy are shown in Fig. 7. These parameters can be correlated with the four effects identified in the examination of the sintering behaviour and microstructure: (i) formation of the secondary phases $LiTiOPO_4$ and $AlPO_4$; (ii) pore elimination, densification and shrinkage; (iii) grain growth and grain size distribution and (iv) crack formation.

The decomposition of LATP into $AlPO_4$ and $LiTiOPO_4$ seems to impact particularly the bulk conductivity σ_b and grain boundary activation energy $E_{a,gb}$. The macroscopic effects of secondary phases, densification, grain growth and cracks affect mainly the Li-ion percolation network, which correlates with grain boundary conductivity σ_{gb} and capacitance C_{gb}.

Discussion of the impact of secondary phase formation on σ_b

The bulk conductivity seems to depend on the amount of secondary phases, which depends on the sintering temperature and Li_3PO_4 amount. The 5 vol% and 10 vol% samples demonstrate a significant drop between 750 °C and 800 °C (Fig. 7a). The bulk conductivities of the pure LATP samples and the 3 vol% samples are, in general, slightly higher than those of the 5 vol% and 10 vol% samples. The correlation between σ_b and the amount of secondary phases can be explained by the decrease of the overall LATP amount in the sample due to decomposition. However, a change in the lattice stoichiometry of LATP in the case of a reaction of LATP with Li_3PO_4 to $AlPO_4$ or $LiTiOPO_4$ is also conceivable and would influence the bulk conductivity. The bulk conductivities of the samples sintered at 950 °C are 1.52×10^{-3} S cm^{-1} ± 0.17×10^{-3} S cm^{-1} (pure LATP), 1.46×10^{-3} S cm^{-1} ± 0.08×10^{-3} S cm^{-1} (3 vol%), 1.23×10^{-3} S cm^{-1} ± 0.12×10^{-3} S cm^{-1} (5 vol%) and 1.19×10^{-3} S cm^{-1} ± 0.32×10^{-3} S cm^{-1} (10 vol%). However, the error is quite high (>6%). Measurements at temperatures <−100 °C, as demonstrated by Breuer *et al.*, would likely give more accurate results due to a shift of the bulk conductivity to lower frequencies and thus, easier separation of the semicircles related to the bulk and grain boundary conductivities.[51] Furthermore, high porosity can influence the impedance data at high frequencies.[23,52] Nevertheless, the bulk conductivities obtained in this study are in good accordance with the literature.[42,51,53]

Discussion of the impact of secondary phase formation on $E_{a,gb}$

A correlation between the Li_3PO_4 amount, sintering temperature and grain boundary activation energy $E_{a,gb}$ can also be detected (Fig. 7d), which suggests that the formation of the secondary phases impacts the energy barrier for Li-ion conduction through the grain boundaries. The LATP + 3 vol% Li_3PO_4 samples show the highest activation energies at all sintering temperatures. Although the difference is low at 950 °C, the influence of Li_3PO_4 is highlighted at 850 °C. The 3 vol%, 5 vol% and 10 vol% samples show values of 403 meV, 387 meV and 366 meV, respectively. Additionally, these activation energies are significantly higher than 341 meV obtained for the pure LATP pellet sintered at 950 °C, which is in good accordance with the literature, where values between 310 meV and 360 meV are reported for pure LATP.[22,51] Consequently, the addition of Li_3PO_4 increases the activation energy, and thus the barrier for Li-ion conduction between grains. However, the counter-intuitive correlation between a higher Li_3PO_4 amount and lower $E_{a,gb}$ values might allow two interpretations: (1) hopping of Li-ions between LATP and the secondary phases or Li_3PO_4 takes place, which is enhanced by larger secondary phase grain sizes; (2) an increased formation of $AlPO_4$ and $LiTiOPO_4$ increases the

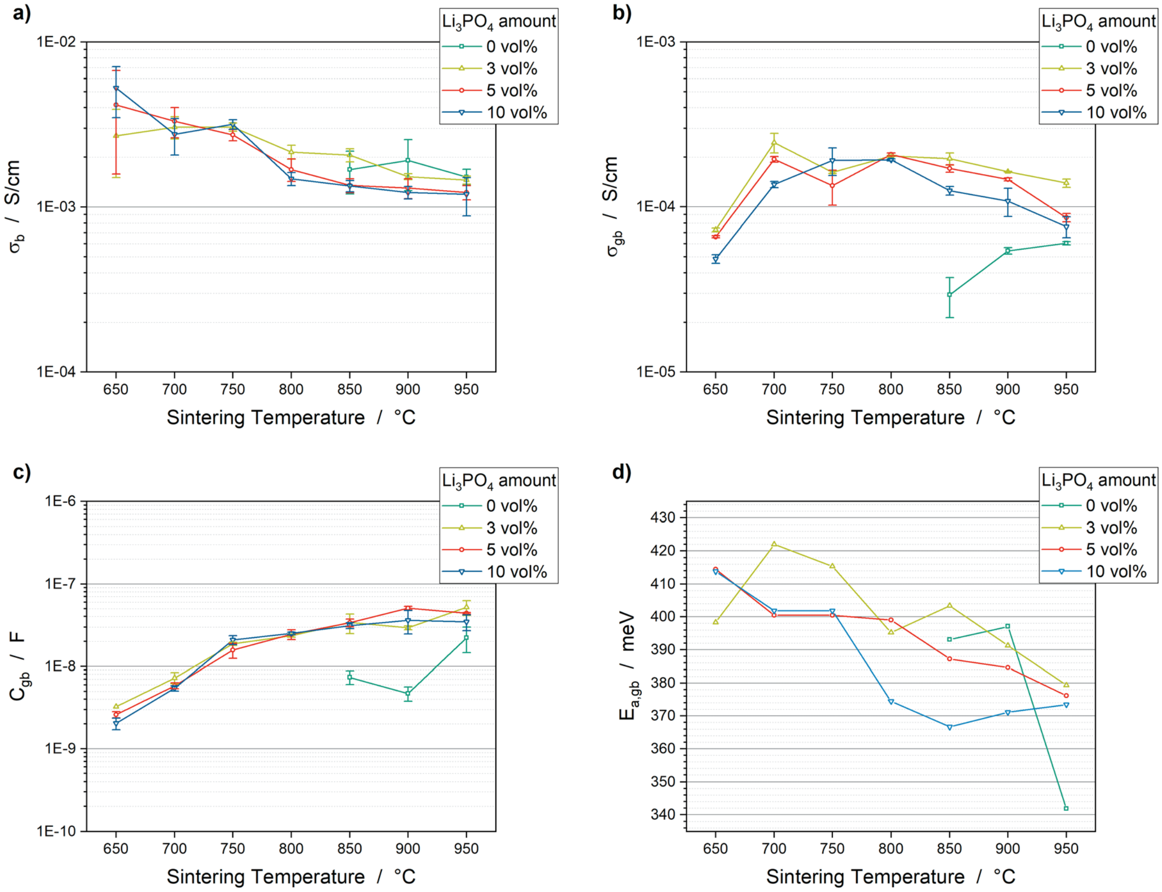

Fig. 7 Electrical properties as a function of the sintering temperature: (a) bulk conductivity, σ_b; (b) grain boundary conductivity, σ_{gb}; (c) grain boundary capacitance, C_{gb}; (d) grain boundary activation energy, $E_{a,gb}$.

misorientation at the grain boundaries between LATP grains due to changes in the stoichiometry in the outer region of the LATP grains. This might increase the thickness of the grain boundary regime, so that it can be seen as a separate phase, in which Li-ions can migrate by passing a lower energy barrier. Although the impact of the Li_3PO_4 amount on $E_{a,gb}$ is evident in this study, an exact description of the hopping mechanism cannot be reliably given. Further investigation by means of atomic-resolution scanning transmission electron microscopy, as demonstrated by Ma *et al.*,[34] needs to be done in order to examine the misorientation at the grain boundaries and its dependency on the Li_3PO_4 amount, so that the two hypotheses can be verified.

Discussion of the impact of macroscopic effects on σ_{gb}

For a reasonable interpretation of the impact of the macroscopic effects, such as densification, grain growth, crack formation and formation of secondary phases, on the grain boundary conductivity, the characteristics of an efficient percolating network should be considered. The possibilities for Li-ion migration need to be increased. This can be realized by maximizing the grain to grain contacts due to densification and pore elimination. Additionally, the grain lattice orientation should also be considered. The LATP NASICON structure is a 3-dimensional conductor, which means that the Li-ion diffusion occurs along three axes in the crystalline material.[54] The lattice planes that correlated with these diffusion tunnels must sufficiently match with the same lattice planes of the neighbouring grains to ensure efficient Li-ion hopping. The possibility of matching lattice planes and the amount of grain to grain contacts are increased with smaller grain sizes. Any disruption of the percolating network, *e.g.* due to cracks, pores, *etc.*, results in a decrease of the overall conductivity. Therefore, the microstructure of the sintered material plays an important role in the conductivity of the material.

Consequently, the significant differences in the microstructures of the pure LATP and the LATP + 5 vol% Li_3PO_4 samples result in significant differences in the grain boundary conductivity. The pure LATP pellet sintered at 950 °C shows a high porosity of 33% (Fig. 4a), grain sizes of >60 μm and the existence of macroscopic cracks through the microstructure (Fig. 5c). These properties affect the percolation network for Li-ion migration, which cause a low grain boundary conductivity of 6.03×10^{-5} S cm^{-1} $\pm$ 0.14×10^{-5} S cm^{-1} (Fig. 7b). Since the final sintering stage of LATP is not reached at 950 °C without a sintering additive, higher values of $>10^{-4}$ S cm^{-1} are expected to be achievable at higher temperatures. Therefore, the grain boundary conductivity of pure LATP is in accordance with values in the literature, considering the sintering temperature and duration.[20,51]

Adding Li_3PO_4 to LATP accelerates the pore elimination (Fig. 4b), so that the grain boundary conductivities of the Li_3PO_4-containing samples sintered at 650 °C are comparable with the values of the pure LATP samples sintered at 950 °C (Fig. 7b). A significant increase in σ_{gb} occur between 650 °C and 700 °C during the intermediate sintering stage for all Li_3PO_4-containing samples (Fig. 7b). A steady decrease of σ_{gb} occurs during the final sintering stage between 800 °C and 950 °C (Fig. 7b). These trends can be explained by the changes in the microstructure represented by porosity, grain size, cracks and secondary phases, which are exemplarily illustrated for the LATP + 5 vol% Li_3PO_4 sample and set side by side with the grain boundary conductivities in Fig. 8.

Pore elimination causes an increase in grain boundary conductivity to 1.94×10^{-4} S cm^{-1} ± 0.07×10^{-4} S cm^{-1} between 650 °C and 700 °C due to an increase of the grain to grain contacts (Fig. 8). However, the porosity of 28% of the 700 °C sintered sample is still high and a further significant reduction to 7% at 800 °C does not cause an expected significant increase in grain boundary conductivity (2.08×10^{-4} S cm^{-1} ± 0.04×10^{-4} S cm^{-1} at 800 °C). Cracks and secondary phases could not be observed for these samples, so the three times higher grain sizes for the upper and lower limit of the grain size distribution might have an impact on the percolation network for Li-ion migration (Fig. 8). The very narrow grain size distribution and grain sizes of *ca.* 2–6 μm at 700 °C seem to form a good percolation network with a high degree of possibilities for Li-ion migration from grain to grain in spite of high porosity. The comparable grain boundary conductivities indicate that this percolation network is comparable with the percolation network formed by *ca.* 6–18 μm grains at 800 °C with lower porosity due to the impact of a higher probability of contact areas with mismatching lattice planes.[20] This trend in σ_{gb} occurs for all Li_3PO_4-containing samples (3 vol%, 5 vol% and 10 vol%, Fig. 7b) with similar grain boundary conductivities of *ca.* 2×10^{-4} S cm^{-2} at 800 °C.

Further grain growth between 800 °C and 950 °C might partly affect the decrease in σ_{gb} to 0.86×10^{-4} S cm^{-1} ± 0.04×10^{-4} S cm^{-1} (950 °C, Fig. 8). In addition to larger grain sizes, the formation of macroscopic cracks as well as the formation of a higher amount of the secondary phases $AlPO_4$ and $LiTiOPO_4$ at higher sintering temperatures interrupt the percolation network, which results in a reduction of the grain boundary conductivity. In particular, the amount of secondary phases appears to depend on the Li_3PO_4 amount (Fig. 1), so the samples with 3 vol% Li_3PO_4 show a lower decrease in grain boundary conductivity to 1.40×10^{-4} S cm^{-1} ± 0.08×10^{-4} S cm^{-1} at 950 °C and the samples with 10 vol% Li_3PO_4 show a higher decrease to 0.76×10^{-4} S cm^{-1} ± 0.11×10^{-4} S cm^{-1} at 950 °C (Fig. 7b).

The Li_3PO_4-containing pellets sintered at 800 °C can be set as a reference point in comparison with the pure LATP pellets, since it shows the lowest porosity and the samples sintered at 750 °C exhibit a high error of 24% in the grain boundary conductivity. This high error can be attributed to the transition from the intermediate to the final sintering stage, which seems to lead to significant variations in the microstructure in the different pellets. Conclusively, adding Li_3PO_4 to LATP results in a possible decrease in sintering temperature by ≥200 °C, at least in terms of the grain boundary conductivity.

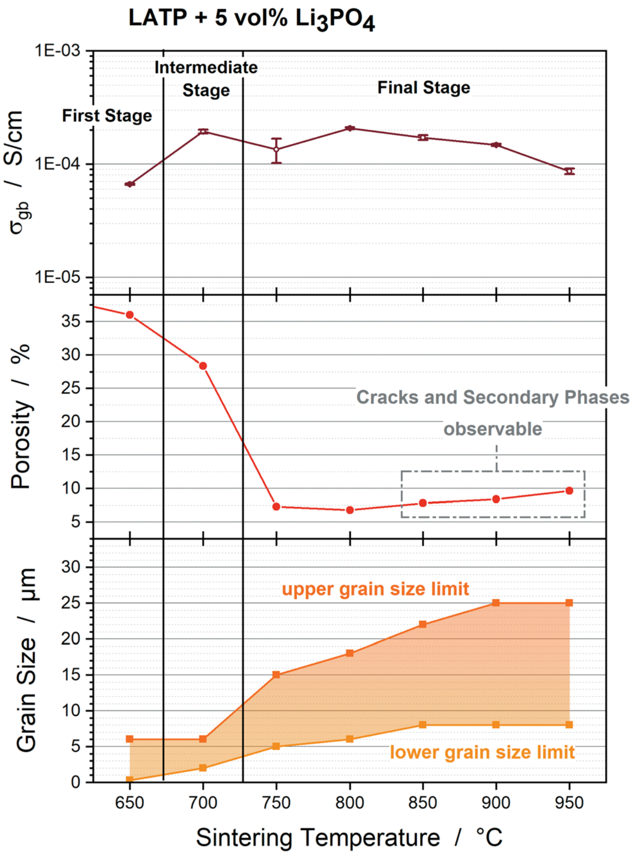

Fig. 8 Comparison of the electrochemical and microstructural results of the LATP + 5 vol% Li_3PO_4 samples as a function of the sintering temperature: grain boundary conductivity (EIS), porosity (Archimedes principle), grain size and observable crack formation (SEM).

Discussion of the impact of macroscopic effects on C_{gb}

The addition of Li_3PO_4 has also an impact on the grain boundary capacitance. When considering the brick-layer model,[28,29,52] grain boundaries can be described as capacitors according to the following equation:

$$C_{gb} = \varepsilon_{gb}\varepsilon_0 \cdot \frac{d_g^{\,2}}{d_{gb}}$$

where the plate area $A_C = d_g^{\,2}$ depends on the grain edge length d_g correlating with grain size, the plate distance is represented by the grain boundary thickness d_{gb} and the permittivity ε_{gb} is associated with the nature of the grain boundary. Since d_g is at least 1000 times higher than d_{gb}, it is expected that the grain size makes the most significant effect on the capacitance. In Fig. 7c, the grain boundary capacitance can be divided into two regions, each with a different slope. The first region with a higher slope can be detected between 650 °C and 750 °C. In this sintering temperature range, the pore elimination increases the amount of grain boundaries and the grain size distribution increases from 0.3–6 μm to 5–15 μm (Fig. 8). In the second region, the grain size undergoes a smaller increase to 8–25 μm at 900 °C, so that the capacitance also exhibits a lower increase to *ca.* 4×10^{-8} F and remains constant at 950 °C for all Li_3PO_4-containing samples. The capacitance of the pure LATP pellets sintered at 950 °C is *ca.* 2×10^{-8} F, which is comparable to the Li_3PO_4-containing samples. Considering the large grain size of > 60 μm, the influence of the permittivities of $AlPO_4$, $LiTiOPO_4$ and Li_3PO_4 cannot be excluded. The change in the grain boundary thickness cannot be determined by the techniques used in this study.

Conclusions

The sintering process of LATP was significantly accelerated by adding Li_3PO_4. Liquid phase sintering reduced the temperatures of sinter neck formation by 50 °C and the start of shrinkage by 150 °C. Furthermore, it limited the maximum grain size. The sintering behaviour of the LATP + 5 vol% Li_3PO_4 mixture could be categorized into three sintering stages by means of the analyses of the densification and grain growth. The final sintering stage is reached at 800 °C in the presence of Li_3PO_4, while the pure LATP samples seem to be still in the intermediate stage at 950 °C. Consequently, improved grain boundary conductivities were achieved at low sintering temperatures. The Li_3PO_4-containing LATP samples sintered at 800 °C show high conductivities of *ca.* 2×10^{-4} S cm^{-1}, which is comparable to the literature values of pure LATP sintered at > 1000 °C.[20,51,53]

A correlation between sintering behaviour, microstructure and electrical properties was elucidated. Four main effects appear during sintering: (i) formation of the secondary phases $LiTiOPO_4$ and $AlPO_4$; (ii) pore elimination, densification and shrinkage; (iii) grain growth and grain size distribution and (iv) crack formation. The formation of the secondary phases can be particularly correlated with the bulk conductivity and the grain boundary activation energy. Densification, grain size, crack formation and the formation of the secondary phases have an impact on the macroscopic characteristics of the Li-ion percolation network. Low porosity and small grain sizes increase the amount of grain to grain contacts, and thus the possibility for Li-ion hopping, which directly improves the grain boundary conductivity. Any interruption of the percolating network, such as crack formation or non-conductive secondary phases, causes a decrease in grain boundary conductivity. It could be shown that smaller grain size has comparable importance to low porosity. In conclusion, the use of Li_3PO_4 as a sintering additive is a promising approach to reduce the sintering temperature and grain size, which concurrently increases the ionic conductivity. Further optimization of the sintering conditions is possible based on the foundation presented here. Decomposition and mixed phase formation during the sintering of ternary cathode layers can probably be inhibited by the reduced sintering temperature, which would be the next step towards a competitive ceramic ASSB.

Conflicts of interest

The authors declare no conflict of interest. The funders had no role in the design of the study; in the collection, analyses, or interpretation of data; in the writing of the manuscript, or in the decision to publish the results.

Acknowledgements

The authors acknowledge Werner Stracke of the cluster services at the Fraunhofer ISC for the preparation and the accomplishment of the scanning electron microscopy analysis. Furthermore, we thank the Center for High Temperature Materials and Design (HTL, Fraunhofer ISC) for the access and accomplishment of the thermal optical measurement devices and the Archimedes based water saturation equipment. The authors acknowledge the financial support from the Bavarian Ministry of Economic Affairs and Media, Energy and Technology for funding the Fraunhofer R & D Center for Electromobility Bavaria FZEB (Grant number: 43-6629/86)

References

1 W. Hou, X. Guo, X. Shen, K. Amine, H. Yu and J. Lu, *Nano Energy*, 2018, **52**, 279–291.
2 Y.-S. Hu, *Nat. Energy*, 2016, **1**, 652.
3 J. Janek and W. G. Zeier, *Nat. Energy*, 2016, **1**, 1167.
4 A. C. Luntz, J. Voss and K. Reuter, *J. Phys. Chem. Lett.*, 2015, **6**, 4599–4604.
5 D. H. S. Tan, A. Banerjee, Z. Chen and Y. S. Meng, *Nat. Nanotechnol.*, 2020, **15**, 170–180.
6 R. C. Xu, X. H. Xia, S. Z. Zhang, D. Xie, X. L. Wang and J. P. Tu, *Electrochim. Acta*, 2018, **284**, 177–187.
7 T. Zhang, W. He, W. Zhang, T. Wang, P. Li, Z. Sun and X. Yu, *Chem. Sci.*, 2020, **334**, 928.
8 F. Zheng, M. Kotobuki, S. Song, M. O. Lai and L. Lu, *J. Power Sources*, 2018, **389**, 198–213.
9 F. Han, Y. Zhu, X. He, Y. Mo and C. Wang, *Adv. Energy Mater.*, 2016, **6**, 1501590.
10 Y. Zhu, X. He and Y. Mo, *ACS Appl. Mater. Interfaces*, 2015, **7**, 23685–23693.
11 Y. Zhu, X. He and Y. Mo, *J. Mater. Chem. A*, 2016, **4**, 3253–3266.
12 K. Kerman, A. Luntz, V. Viswanathan, Y.-M. Chiang and Z. Chen, *J. Electrochem. Soc.*, 2017, **164**, A1731–A1744.
13 M. Gellert, E. Dashjav, D. Grüner, Q. Ma and F. Tietz, *Ionics*, 2018, **24**, 1001–1006.
14 L. J. Miara, W. D. Richards, Y. E. Wang and G. Ceder, *Chem. Mater.*, 2015, **27**, 4040–4047.
15 M. Rumpel, F. Nagler, L. Appold, W. Stracke, A. Flegler, O. Clemens and G. Sextl, *Mater. Adv.*, 2022, **52**, 279.

16 Z. Z. Fang, *Sintering of advanced materials. Fundamentals and processes*, Woodhead Pub, Oxford, Philadelphia, PA, 2010.
17 S.-J. L. Kang, *Sintering. Densification, grain growth, and microstructure*, Elsevier, Amsterdam, 2005.
18 H. Salmang, H. Scholze and R. Telle, *Keramik (German Edition)*, Springer, Dordrecht, 2007.
19 Q. Yin, B. Zhu and H. Zeng, *Microstructure, property and processing of functional ceramics*, Metallurgical Industry Press, Springer Verlag, Berlin, 2009.
20 T. Hupfer, E. C. Bucharsky, K. G. Schell, A. Senyshyn, M. Monchak, M. J. Hoffmann and H. Ehrenberg, *Solid State Ionics*, 2016, **288**, 235–239.
21 S. Indris, P. Heitjans, H. E. Roman and A. Bunde, *Phys. Rev. Lett.*, 2000, **84**, 2889–2892.
22 S. D. Jackman and R. A. Cutler, *J. Power Sources*, 2012, **218**, 65–72.
23 H. Keiser, K. D. Beccu and M. A. Gutjahr, *Electrochim. Acta*, 1976, **21**, 539–543.
24 P. Knauth, *Solid State Ionics*, 2006, **177**, 2495–2502.
25 C. R. Mariappan, C. Yada, F. Rosciano and B. Roling, *J. Power Sources*, 2011, **196**, 6456–6464.
26 K. G. Schell, E. C. Bucharsky, F. Lemke and M. J. Hoffmann, *Ionics*, 2017, **23**, 821–827.
27 K. Waetzig, A. Rost, C. Heubner, M. Coeler, K. Nikolowski, M. Wolter and J. Schilm, *J. Alloys Compd.*, 2020, **818**, 153237.
28 R. Bouchet, P. Knauth and J.-M. Laugier, *Solid State Ionics*, 2003, **150**, E348.
29 R. Bouchet, P. Knauth and J.-M. Laugier, *J. Electroceram.*, 2006, **16**, 229–238.
30 J. Fleig, *Solid State Ionics*, 1998, **113–115**, 739–747.
31 J. Fleig, *Solid State Ionics*, 2000, **131**, 117–127.
32 J. Fleig and J. Maier, *J. Eur. Ceram. Soc.*, 1999, **19**, 693–696.
33 J. Maier, *Prog. Solid State Chem.*, 1995, **23**, 171–263.
34 C. Ma, K. Chen, C. Liang, C.-W. Nan, R. Ishikawa, K. More and M. Chi, *Energy Environ. Sci.*, 2014, **7**, 1638.
35 H. Aono, E. Sugimoto, Y. Sadaoka, N. Imanaka and G. Adachi, *Solid State Ionics*, 1991, **47**, 257–264.
36 K. Chen, M. Huang, Y. Shen, Y. Lin and C. W. Nan, *Electrochim. Acta*, 2012, **80**, 133–139.
37 K. Chen, M. Huang, Y. Shen, Y. Lin and C. W. Nan, *Solid State Ionics*, 2013, **235**, 8–13.
38 T. Hupfer, E. C. Bucharsky, K. G. Schell and M. J. Hoffmann, *Solid State Ionics*, 2017, **302**, 49–53.
39 Y. Kobayashi, M. Tabuchi and O. Nakamura, *J. Power Sources*, 1997, **68**, 407–411.
40 A. Mei, X. Wang, Y. Feng, S. Zhao, G. Li, H. Geng, Y. Lin and C. Nan, *Solid State Ionics*, 2008, **179**, 2255–2259.
41 A. Mei, X.-L. Wang, J.-L. Lan, Y.-C. Feng, H.-X. Geng, Y.-H. Lin and C.-W. Nan, *Electrochim. Acta*, 2010, **55**, 2958–2963.
42 K. Waetzig, C. Heubner and M. Kusnezoff, *Crystals*, 2020, **10**, 408.
43 Alfa Aeasar, 2009.
44 F. Raether, R. Hofmann, G. Müller and H. J. Sölter, *J. Therm. Anal. Calorim.*, 1998, **53**, 717–735.
45 F. Raether and R. Springer, *Adv. Eng. Mater.*, 2000, **2**, 741–744.
46 J. Baber, A. Klimera and F. Raether, *J. Eur. Ceram. Soc.*, 2007, **27**, 701–705.
47 L. Stanciu, D. Quach, C. Faconti, J. R. Groza and F. Raether, *J. Am. Ceram. Soc.*, 2007, **90**, 2716–2722.
48 L. Stanciu, D. Quach, C. Faconti, J. R. Groza and F. Raether, *J. Am. Ceram. Soc.*, 2007, **90**, 2716–2722.
49 K. Waetzig, A. Rost, U. Langklotz, B. Matthey and J. Schilm, *J. Eur. Ceram. Soc.*, 2016, **36**, 1995–2001.
50 S. Duluard, A. Paillassa, L. Puech, P. Vinatier, V. Turq, P. Rozier, P. Lenormand, P.-L. Taberna, P. Simon and F. Ansart, *J. Eur. Ceram. Soc.*, 2013, **33**, 1145–1153.
51 S. Breuer, D. Prutsch, Q. Ma, V. Epp, F. Preishuber-Pflügl, F. Tietz and M. Wilkening, *J. Mater. Chem. A*, 2015, **3**, 21343–21350.
52 E. Barsoukov and J. R. Macdonald, *Impedance spectroscopy. Theory, experiment, and applications*, Wiley-Interscience, Hoboken N.J., 2nd edn, 2005.
53 R. DeWees and H. Wang, *ChemSusChem*, 2019, **12**, 3713–3725.
54 Y. Ren, K. Chen, R. Chen, T. Liu, Y. Zhang and C.-W. Nan, *J. Am. Ceram. Soc.*, 2015, **98**, 3603–3623.